Electronic Supplementary Material (ESI) for Nanoscale.
This journal is © The Royal Society of Chemistry 2021

Electronic supplementary information

In-situ Formation of Grain Boundaries on Supported Hybrid to Boost Water Oxidation Activity of Iridium Oxide

Wei Sun[a,], Zhiqiang Wang[b], Xinlong Tian[c], Hui Deng[a], Jianjun Liao[a] , Chenglong Ma[d], Ji Yang[d], Xueqing Gong[b], Weiwei Huang[a,*] and Chengjun Ge[a,*]*

a. Key Laboratory of Agro-Forestry Environmental Processes and Ecological Regulation of Hainan Province, College of Ecology and Environment, Hainan University, 58 Renmin Road, Haikou 570228, P.R. China.

b. Key Laboratory for Advanced Materials, Center for Computational Chemistry and Research Institute of Industrial Catalysis, East China University of Science and Technology, 130 Meilong Road, Shanghai 200237, P. R. China.

c. State Key Laboratory of Marine Resource Utilization in South China Sea, Hainan University, 58 Renmin Road, Haikou 570228, P.R. China.

d. State Environmental Protection Key Laboratory of Environmental Risk Assessment and Control on Chemical Processes, School of Resources and Environmental Engineering, East China University of Science and Technology, 130 Meilong Road, Shanghai 200237, P.R. China.

* Weiwei Huang: huang05106114@163.com; Chengjun Ge: cjge3007@163.com

KEYWORDS: Water oxidation; Supported hybrid; Ultrafine nanoparticles; IrO_2; Grain boundary.

METHODS

Material preparation

Materials: All chemicals and solvents used in the experiments were of analytical grade and used without additional purification. The iridium (IV) chloride ($H_2IrCl_6 \cdot 6H_2O$), manganese sulfate (Mn_2SO_4), potassium permanganate ($KMnO_4$), manganese nitrate ($Mn(NO_3)_2$), ammonium persulfate ($(NH_4)_2S_2O_8$), hydrochloric acid (HCl), sodium hydroxide (NaOH), perchloric acid ($HClO_4$) were all purchased from Macklin Co. Ltd., China. De-ionized water (18.2 MΩ) without further purification was prepared from laboratory and used in preparing different solution.

Preparations of different Mn-based oxides support: The β-MnO_2 support was prepared by oxidized the low valence state of Mn^{2+} in the presence of oxidant via hydrothermal method, which inspired by previous reported[1]. In a typically, 5 mL (0.1M) Mn_2SO_4 solution was added into 20 mL aqueous, which containing 0.01 mmol $(NH_4)_2S_2O_8$. The mixture was then transferred to a 50 mL Teflon-lined stainless-steel autoclave and heated at 180 ºC in an oven for 12 h. The precipitates were suction-filtered and washed with deionized water twice to remove other ions. The α-MnO_2 support was prepared via the hydrothermal synthesis process reported in previous studies[2-4]. The reagents contain 0.1 M manganese sulfate (Mn_2SO_4) and 0.1 M potassium permanganate ($KMnO_4$) in aqueous solution with a molar ratio of 0.37 (Mn^{2+}/Mn^{7+}). Then, an additional 15 mL of deionized water is mixed into the solution, transferred to a 50-mL Teflon-lined pressure vessel and loaded into an oven to heat the solution to 150 °C for 12h. The support of cryptomelane (K_xMnO_2, k-Mn) was prepared according to our previous reported[5], 0.1 M of 6 mL $KMnO_4$ solution was mixed with 0.5 mL 0.5 M HCl and later 15 mL deionized water is added, and then be transferred to a 50-mL Teflon-lined pressure vessel and loaded into an oven to heat the solution to 200 °C for 8h. The follow-up purifications are same to previous Mn-based oxides.

IrO_2 supported hybrid: Firstly, weighing different mass of the prepared Mn-based solid to add into 20 mL 0.1M NaOH solution and the mixture was ultrasonicated for at least 30 min to ensure that it was homogenized. Subsequently, according to the design requirements, different volumes of $H_2IrCl_6 \cdot 6H_2O$ (20 mg/mL) precursor was added into the solution. Then, the samples were transferred into a 50 mL Teflon-lined pressure vessel and ultrasonicated for approximately 10 min to form a homogeneous solution. The vessel reactors were placed in an oven and heated at 150 °C for 12 h. The precipitates were suction-filtered and washed with deionized water twice to remove the impurities. The remaining solid on the filter membrane was dried in an oven at 60 °C for at least 30 min. Finally, the obtained powders are annealed at 400 °C for 6 h. All IrO_2 supported hybrid were prepared in the same way.

Crystalline and amorphous IrO_2: 4 mL of 20 mg/L $H_2IrCl_6 \cdot 6H_2O$ precursor was added into 20 mL of 0.1 M NaOH solution. Then, the mixture solution was transferred into a 50 mL Teflon-lined pressure vessel and heated in an oven at 150 °C for 12 h. Subsequent purification process was consistent with the preparation method of IrO_2 supported hybrid. To prepare crystalline and amorphous IrO_2, the iridium oxides solid were annealed at 400 °C (IrO_2-cry) and without any annealing process (IrO_2-un).

Electrode preparation and Electrochemical Measurements

The electrodes used for the electrochemical measurements were prepared as follows. First, 6 mg of fresh catalyst powder was dispersed into a solution mixed with 1.5 mL of 2:1 v/v isopropanol/water

and 15 μL of Nafion. Then the solution was ultrasonicated for approximately 30 min to achieve homogeneity. Next, 7.5 μL of the homogenized solution was deposited on a tailored Ti plate with dimensions of 0.5 cm × 1.5 cm. The Ti plate was etched for 2 h by 10% (wt %) oxalic acid under near boiling conditions. The deposition process was repeated 5 times to obtain a loading weight of approximately 0.2 mg cm^{-2}.

Electrochemical tests were performed in a three-electrode system. Here, a saturated calomel electrode (SCE) was employed as the reference, and a polished and cleaned Pt foil with a 1.5 cm × 1 cm reaction area was used as the counter electrode. The electrode potential from the SCE scale was converted into the reversible hydrogen electrode (RHE) scale by calibration with an equation: $E\ (RHE) = E\ (SCE) + E_{j=0}$. The over-potential values (η) corrected with the iR were calculated using the following equation: $\eta = E_{Applied}$ (RHE)-iR-1.229. The SCE was calibrated with respect to the RHE in all three types of pH solutions using a high purity hydrogen saturated electrolyte with a Pt foil as the working electrode. Cyclic voltammetry (CV) experiments were performed at a scan rate of 1 mV/s, and the average value of the two potentials at which the current crossed zero was recorded as the thermodynamic potential for the hydrogen electrode reaction.

The working electrodes were cycled at least 20 times until the curves overlapped in the CV experiments; then the CV data and polarization curves were recorded at the specified electrochemical measurements. For evaluation the electrochemical surface area of synthesized materials, the prepared electrodes were determined in 0.1 M $HClO_4$ solution with different scan rate. The OER activity with iR-compensation was detected by the linear scan voltammetry (LSV) method under the 10 mV s^{-1}. The solution resistance is determined by the electrochemical impedance spectroscopy (EIS), which was conducted at 1.30 V vs. SCE with a sinusoidal voltage of 10 mV and a frequency ranging from 1 to 10^6 Hz. According to the Nyquist plots from the EIS spectra, the solution resistance in all the electrodes is approximately 8-12 Ω. The stability tests were conducted under the 0.1 M $HClO_4$ solution by the chronopotentiometric method at current density of 10 mA cm^{-2}.

Materials Characterization

The crystal structure of the catalysts was investigated using powder X-ray diffraction (XRD) equipped with a D/max2550 V apparatus and a Cu-Kα radiation source (λ=1.5406 Å), and the data were recorded from 10 to 80° at the step size of 0.02°. A JEM-2100 transmission electron microscope (TEM) was used to characterize the surface morphology. Compositions of the materials were determined by Energy dispersive X-ray (EDX) spectrometer using a TEAMApollo system. The surface properties of the catalysts were determined via X-ray photoelectron spectroscopy (XPS) using an ESCALAB 250Xi instrument with Al-Kα radiation source at an energy step size of 0.05 eV to obtain high-resolution XPS spectra. The samples were sputter-coated with carbon, and the spectra were calibrated with respect to C-*1s* at the binding energy of 284.6 eV. The X-ray absorption (XAS) data of the samples were recorded at room temperature in transmission mode using ion chambers in the Shanghai Synchrotron Radiation Facility[6] (SSFR, beamline BL14W1, Shanghai) and National Synchrotron Radiation Laboratory (NSRL, beamline BL11U, Hefei), China. In order to keep the sample thickness consistent, the overall mass reach 50 mg by adding LiF. The station was operated with a Si (111) double crystal monochromator. During measurements, the synchrotron was operated at the energy of 3.5 GeV and the current varied between 150and 210 mA.

Morlet wavelet transform

In this work, the following Morlet wavelet model was used:

$$\psi(t) = \frac{1}{\sqrt{2\pi}\sigma}\left(\exp(i\kappa t) - \exp(-\frac{\kappa^2}{2})\right)\exp(-\frac{t^2}{2\sigma^2})$$

Where κ and σ are the free parameters in program. The resolution between *k*-space and *R*-space is determined by the parameters of κ and σ. In the M-WT, the larger the value of κ, the higher resolution of *R*-space, which will be very close to the EXAFS spectra. In contrary, lowing the value of κ will obtain to a high resolution of *k*-space. In this work, for a high resolution of *R*-space, we used the parameters of κ and σ are the 15 and 1, respectively. For a good resolution of k-space, the parameters are the 7.5 and 0.5, respectively.

Computational methodology

Density functional theory (DFT) calculations were carried out using the Vienna Ab-initio Simulation Package (VASP)[7]. The spin-polarized projector augmented wave (PAW) method[8] and the Perdew-Burke-Ernzerhof (PBE)[9] electron exchange-correlation functional of the generalized gradient approximation (GGA)[10] were applied in our calculations. The kinetic energy cut-off for the wave function expanded in the plane-wave basis was set as 400 eV. To optimize the structures, the calculation was performed until the maximum force upon each relaxed atom was less than 0.05 eV/Å. The optimized bulk lattice constant for IrO_2 were determined to be a=4.510, b=4.510 and c=3.172 Å, in good agreement with the experimental value of a=4.505, b=4.505 and c=3.159 Å[11]. The vacancy formation energy (E_{vac}) is the energy needed for removing one oxygen atom from the surface to form $1/2O_2$ in the gas-phase. The vacancy formation energy was calculated as follows:

$$E_{vac} = E_v + 1/2E_{O2} - E_{total}$$

where E_{total} is the calculated total energy of the stoichiometric slab, E_{O2} is the total energy of O_2 in gas-phase and E_v is the total energy of a relaxed, defective IrO_2 slab having one O-vacancy in the surface of the supercell.

FIGURES and TABLES

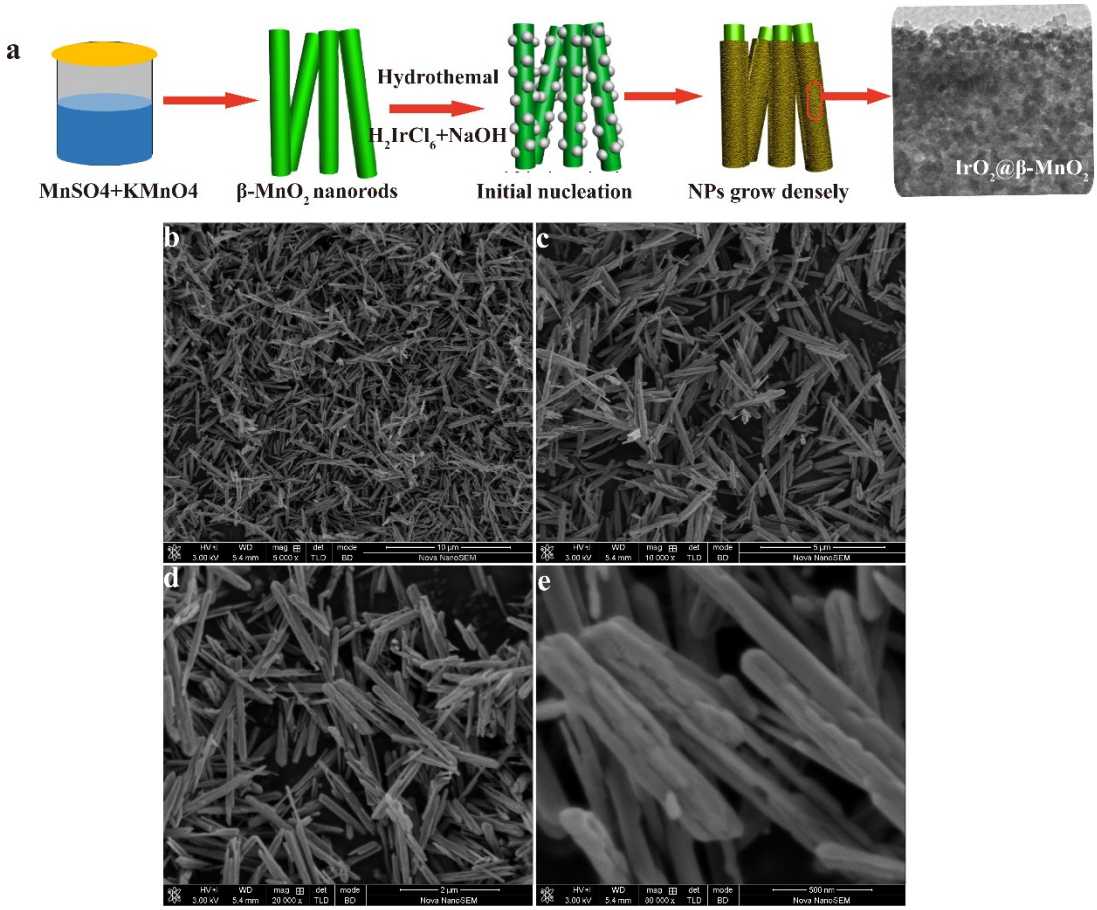

Figure S1. (a) Schematic of preparation of IrO_2 supported hybrid with β-MnO_2 as substrates via two-step hydrothermal processes. (b)-(e) Morphology of synthesized β-MnO_2 by SEM images with different magnifications. The prepared β-MnO_2 belongs to rod-like structure, the rod length range of 0.3 um to 2 um.

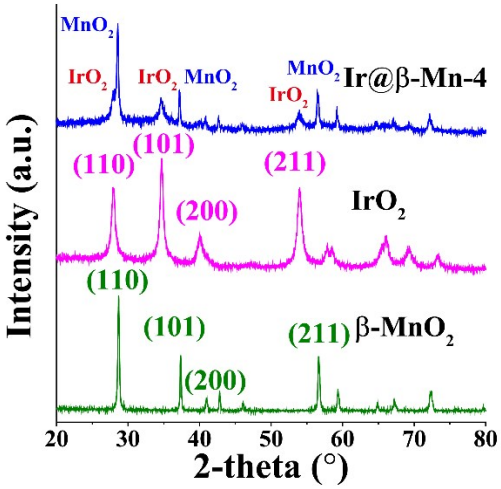

Figure S2. Identifying the crystal diffraction peak of Ir@β-Mn-4, also together with pure IrO_2 and β-MnO_2.

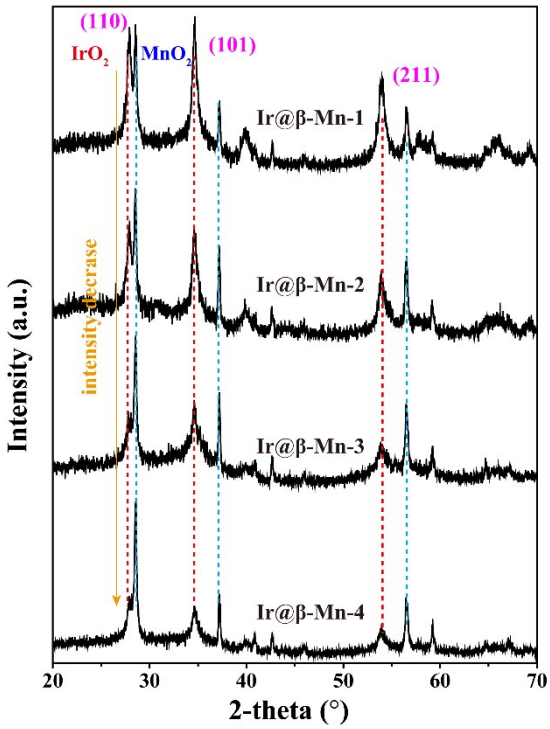

Figure S3. XRD patterns of prepared Ir@Mn hybrid with different growth mass of IrO_2. Both of IrO_2 and β-MnO2 are the rutile structure. Three typical diffraction peaks, (110), (101) and (211), can be used to identify their crystal structures.

Table S1. The feed number of precursors for preparing the Ir@β-Mn hybrid and corresponding to the bulk composition analysis by EDS.

Catalysts	Add volume of H_2IrCl_6 (mL)	Add mass of β-MnO_2 (mg)	Theoretical Ir/Mn bulk atomic ratio[a]	Ir mass ratio (%) by EDS	Ir/Mn bulk atomic ratio by EDS
IrO_2-cry	4	\	\	85.6	\
Ir@β-Mn-1	3	10	1.01	70.2	1.06
Ir@β-Mn-2	3	15	0.67	64.3	0.69
Ir@β-Mn-3	3	20	0.51	53.8	0.54
Ir@β-Mn-4	1.5	20	0.25	37.6	0.27

[a] The equation of $\gamma = (c \times V \times \rho)/192/(m/87)$, is employed to calculating the theoretical Ir/Mn bulk atomic ratio, where *c*-the concentration of Ir precursor (20 mg mL^{-1}), *V*-the added volume of Ir precursor (mL), *ρ*-the quality content of Ir in $H_2IrCl_6 \cdot 6H_2O$ (0.372), *m*-the mass of added β-MnO_2 (mg). 192-the relative atomic mass of Ir (g mol^{-1}), 87-the molecular mass of β-MnO_2 (g mol^{-1})

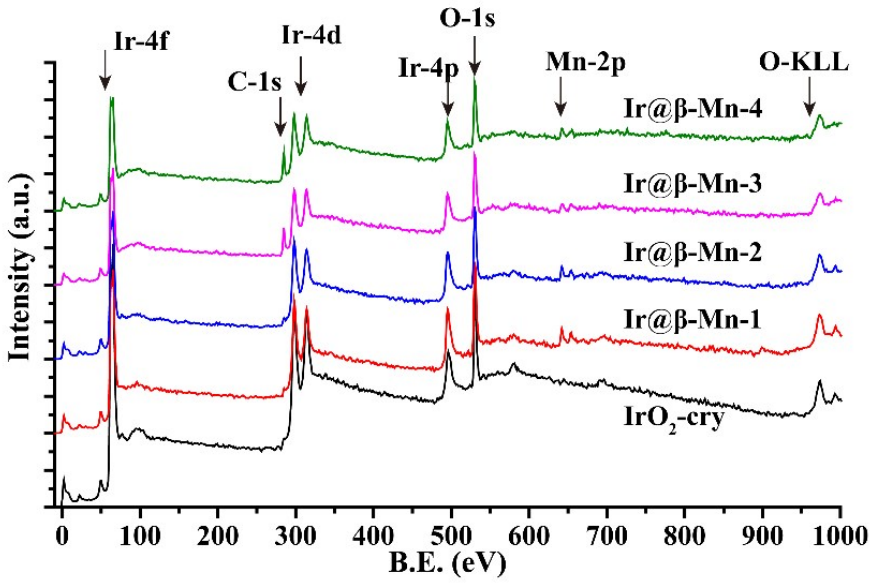

Figure S4. Full spectrum of XPS for the prepared Ir@β-Mn hybrid and together with IrO_2-cry.

Table S2. The surface compositions of prepared Ir@Mn hybrid by XPS elements analysis.

Catalysts	C-1s (atomic, %)	O-1s (atomic, %)	Mn-2$p_{3/2}$ (atomic, %)	Ir-4$f_{7/2}$ (atomic, %)	Ir/Mn atomic ratio
RSF	0.314	0.733	1.757	3.124	
Corrected RSF	28.96	32.99	178.23	156.26	
IrO_2-cry	8.05	74.86	\	17.27	\
Ir@β-Mn-1	6.43	77.84	3.74	11.79	3.15
Ir@β-Mn-2	8.43	76.74	3.93	10.89	2.77
Ir@β-Mn-3	26.69	57.58	4.91	10.81	2.20
Ir@β-Mn-4	30.74	57.86	3.49	7.92	2.27

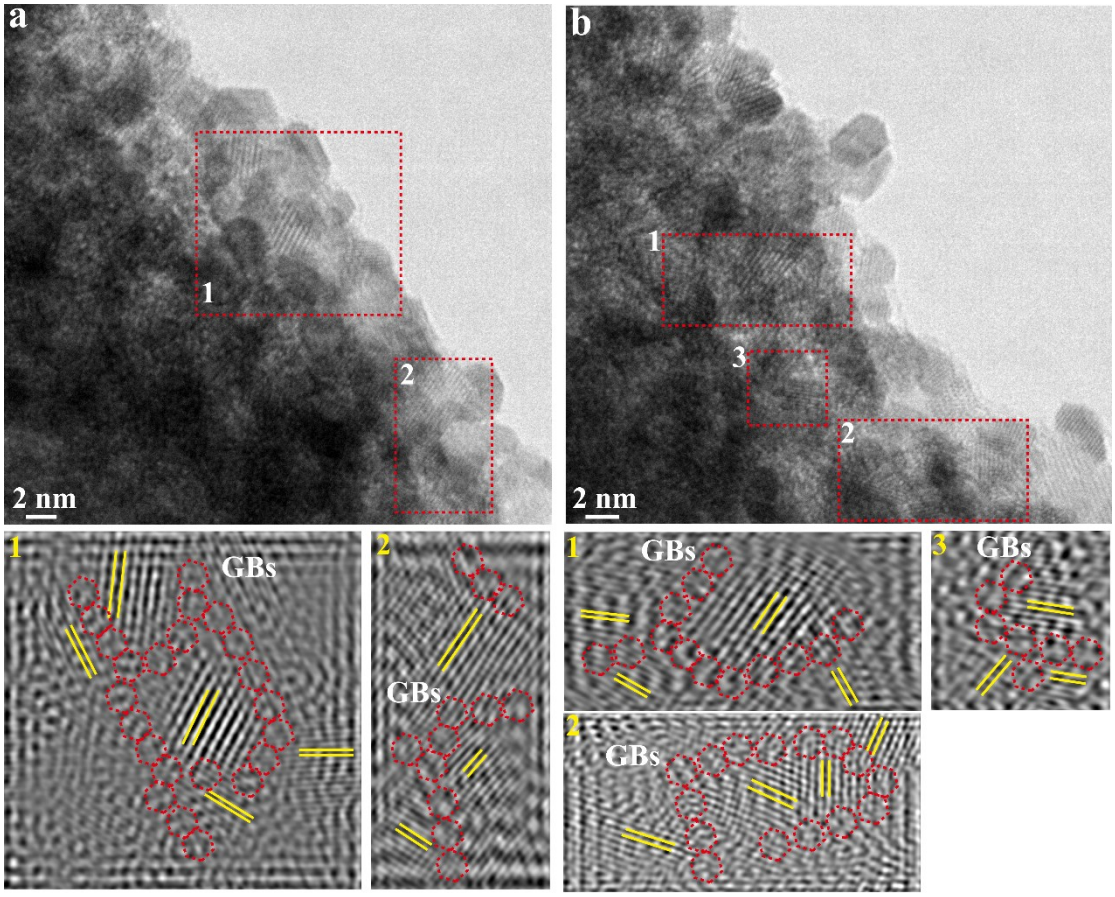

Figure S5. (a) and (b) are HRTEM and their IFFTs images of the prepared Ir@β-Mn-4. From the HRTEM, we can find that large amount of ultrafine IrO_2 NPs with different termination surface randomly linked together. According to the IFFTs images, the lattice fingers of grains on different exposed surfaces are indistinct, which indicates that a large number of GBs are created, and the width of GBs is about several nanometers.

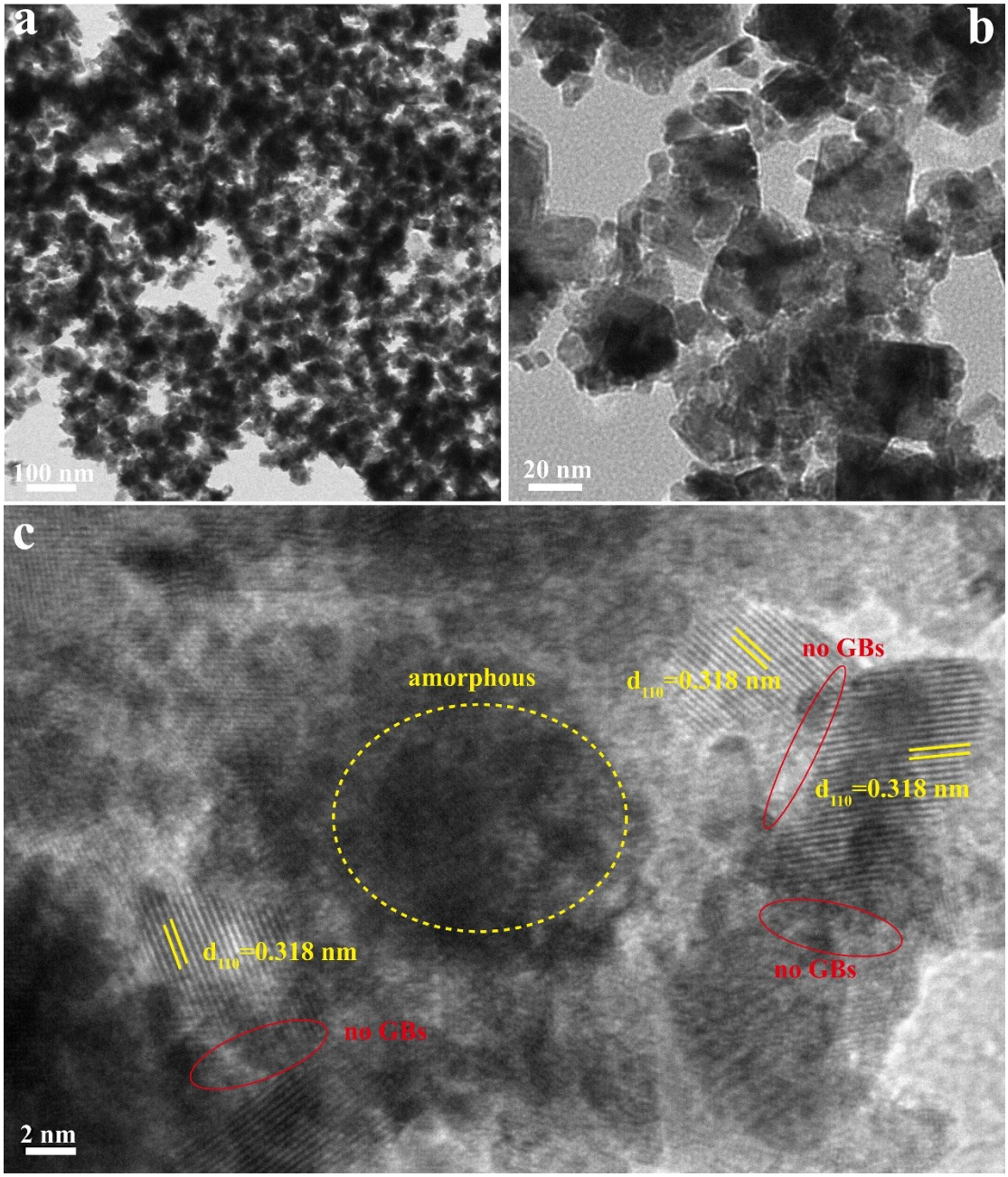

Figure S6. (a) and (b) are TEM images of the prepared IrO_2-cry, who calcined on the 400 ºC for 6 h. (c) HRTEM of IrO_2-cry, we can find that there is no obvious GBs between grains.

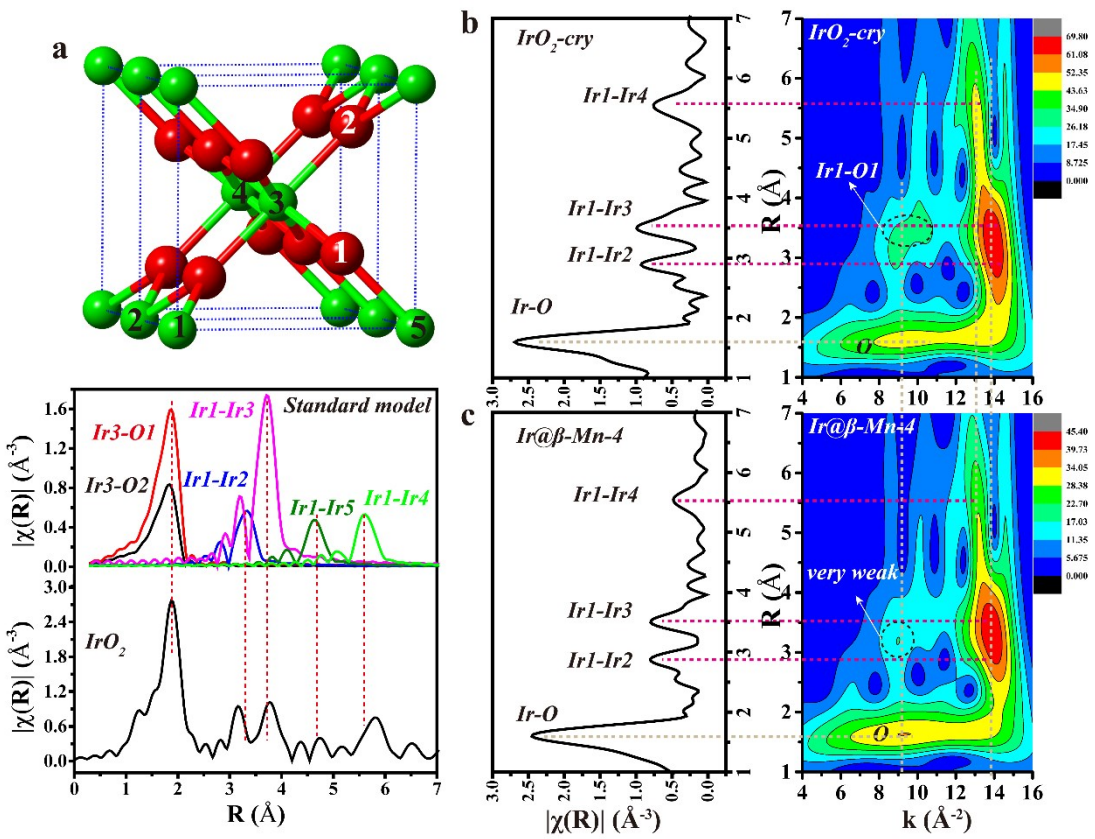

Figure S7. (a) The FT-EXFAS spectra of standard IrO_2. The upper is crystallography of IrO_2. The calculated scattering paths are based from the IrO_2.cif data[11]. IrO_2 parameters are a=b=4.5051 Å, c=3.1586 Å, space=P42/mnm, Ir-O_2=1.9604 Å; Ir-O_4=1.9988 Å. The standard model is composed by 7 clusters of IrO_2 unit cell. The bottom FT-EXAFS is the IrO_2-cry, k range are the 2-14 Å, and be phase corrected. (b) and (c) are the FT-EXFAS spectra and M-WT images of IrO_2-cry and Ir@β-Mn-4, respectively. The k range are the 2-14 Å, and be phase corrected. The parameters of M-WT are set with κ=7.5 and σ=0.5. R range is 0-10 Å.

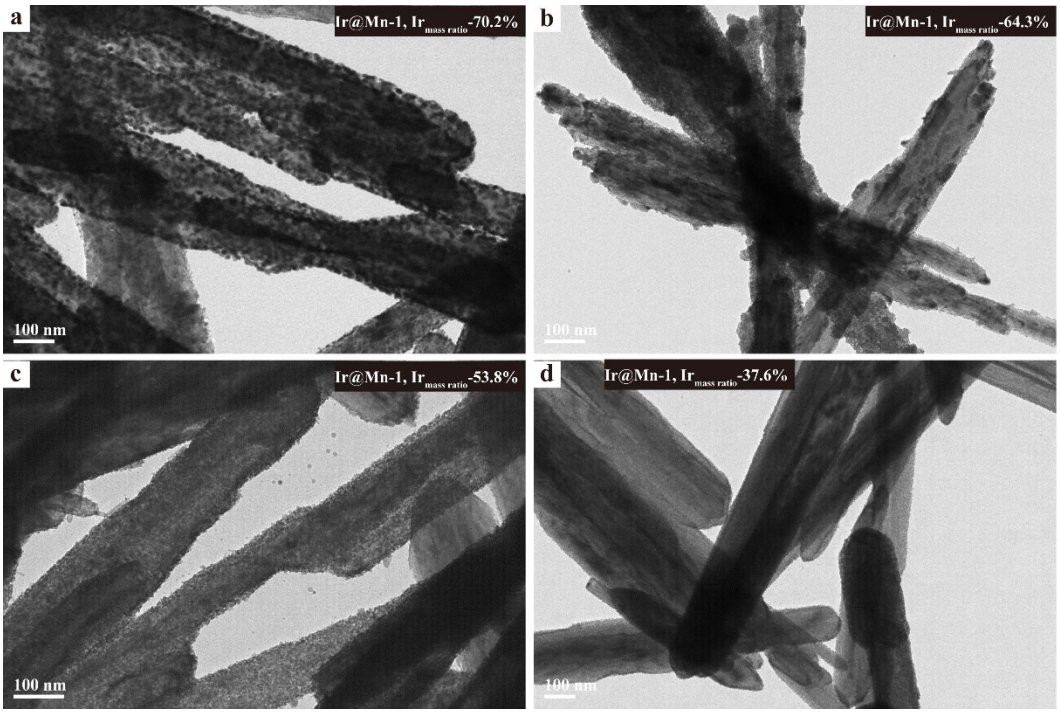

Figure S8. TEM images of series of prepared Ir@β-Mn hybrid. The size of IrO_2 NPs decreased with the decrease of feed Ir/Mn mole ratio.

Table S3. The fitting results of O-1s XPS spectra for different catalysts[a].

Catalysts	O_{Mn-O}			O_{Ir-O}			O_{OH}			O_{H_2O}		
	Percentage (%)	FWHM	GL	Percentage (%)	FWHM	GL	Percentage (%)	FWHM	GL	Percentage (%)	FWHM	GL
IrO_2-un	\	\	\	18.2	1.43	0	58.5	1.64	26	18.5	2.00	69
IrO_2-cry	\	\	\	60.0	1.35	0	19.8	1.27	0	11.7	1.72	0
Ir@β-Mn-4	23.3	1.44	0	28.4	1.29	0	27.2	1.29	0	13.4	1.33	0
β-MnO_2	83.6	1.27	0	\	\	\	11.0	1.32	0	5.4	1.82	0

[a] Percentage (%)-the specific peak area divided by all peaks area. GL- Peak shape function, Gaussian-Lorenz, 0 is 100% Gaussian, 100 is 100% Lorenz.

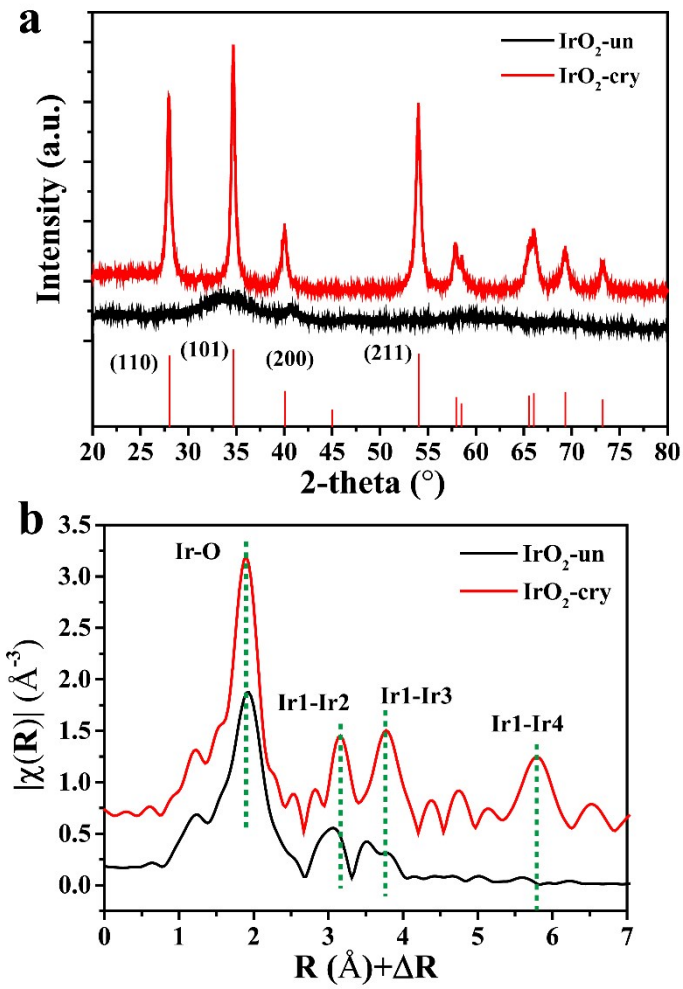

Figure S9. (a) and (b) are the XRD patterns and FT-EXFAS spectra of IrO_2-cry and IrO_2-un, respectively. In the case of IrO_2-un, there is no typical diffraction peaks of rutile structure. The scattering paths of Ir1-Ir3 and Ir1-Ir4 in IrO_2-un are also weaker than that of IrO_2-cry. From the structure comparison, we can conclude that the IrO_2-un belongs to amorphous.

Table S4. The fitting results of Ir-4f XPS spectra for different catalysts.

Catalysts	$4f_{7/2}$-Ir_{Ir-O}			$4f_{7/2}$-Ir_{Ir-OH}			S ratio
	Percentage (%)	FWHM	FWHM	Percentage (%)	FWHM	FWHM	
IrO_2-un	12.3	0.94	84	21.1	1.11	12	**1.71**
IrO_2-cry	28.8	1.05	44	8.5	1.01	0	**0.29**
Ir@β-Mn-4	21.8	0.868	45	12.8	1.07	0	**0.58**

S ratio is the ratio of the area of $4f_{7/2}$-Ir_{Ir-OH} to the area of $4f_{7/2}$-Ir_{Ir-O}.

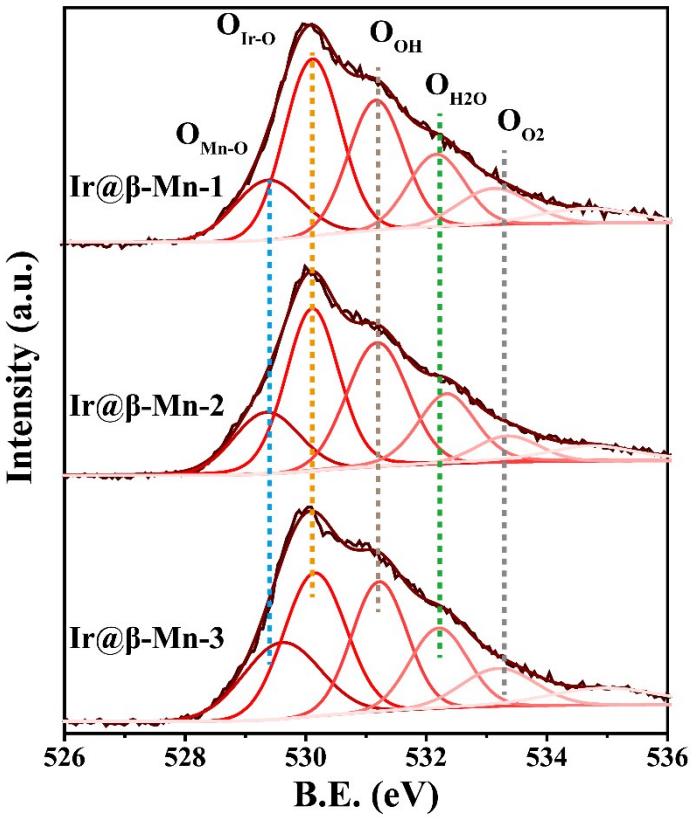

Catalysts	O_{Mn-O} (%)	O_{Ir-O} (%)	O_{OH} (%)	O_{H_2O} (%)
Ir@β-Mn-1	13.9	34.2	24.6	13.9
Ir@β-Mn-2	14.1	32.3	26.3	15.5
Ir@β-Mn-3	18.7	28.4	26.9	13.7

Figure S10. The XPS spectra of O-1s for prepared Ir@β-Mn hybrid. The binding energy is calibrated by C-1s with 284.6 eV. The Table placed on the bottom shows the area percentage of different O-species.

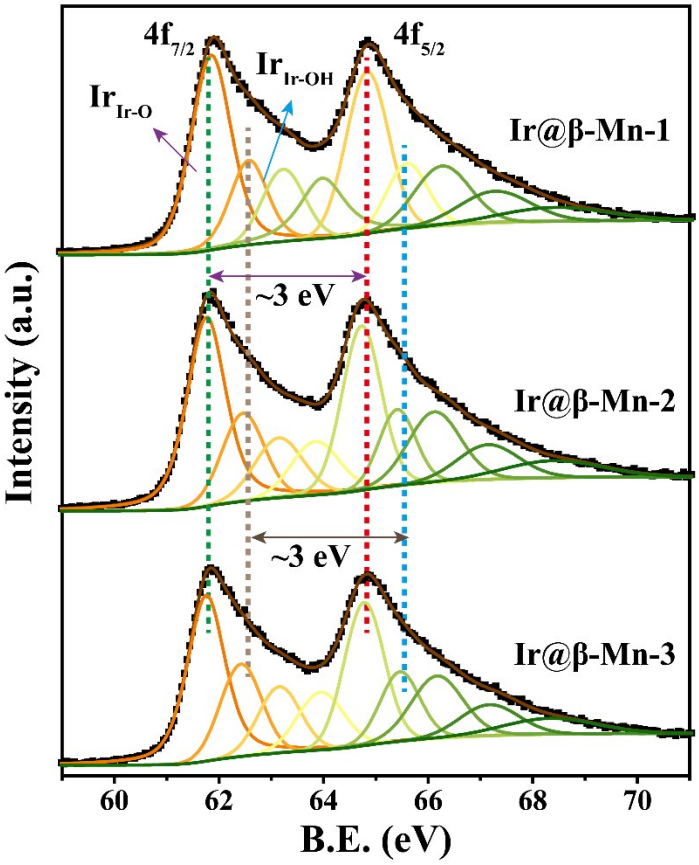

Catalysts	Ir^{4+}_{Ir-O}-$4f_{7/2}$	Ir^{3+}_{Ir-OH}-$4f_{7/2}$	S ratio (%)
Ir@β-Mn-1	12680	4927	28
Ir@β-Mn-2	12486	5307	30
Ir@β-Mn-3	10680	5252	33

Figure S11. The XPS spectra of Ir-4f for prepared Ir@β-Mn hybrid. The binding energy is calibrated by C-1s with 284.6 eV. The Table placed on the bottom shows the area and the area ratio (S ration, %) between Ir^{3+}_{Ir-OH} and Ir^{4+}_{Ir-O}.

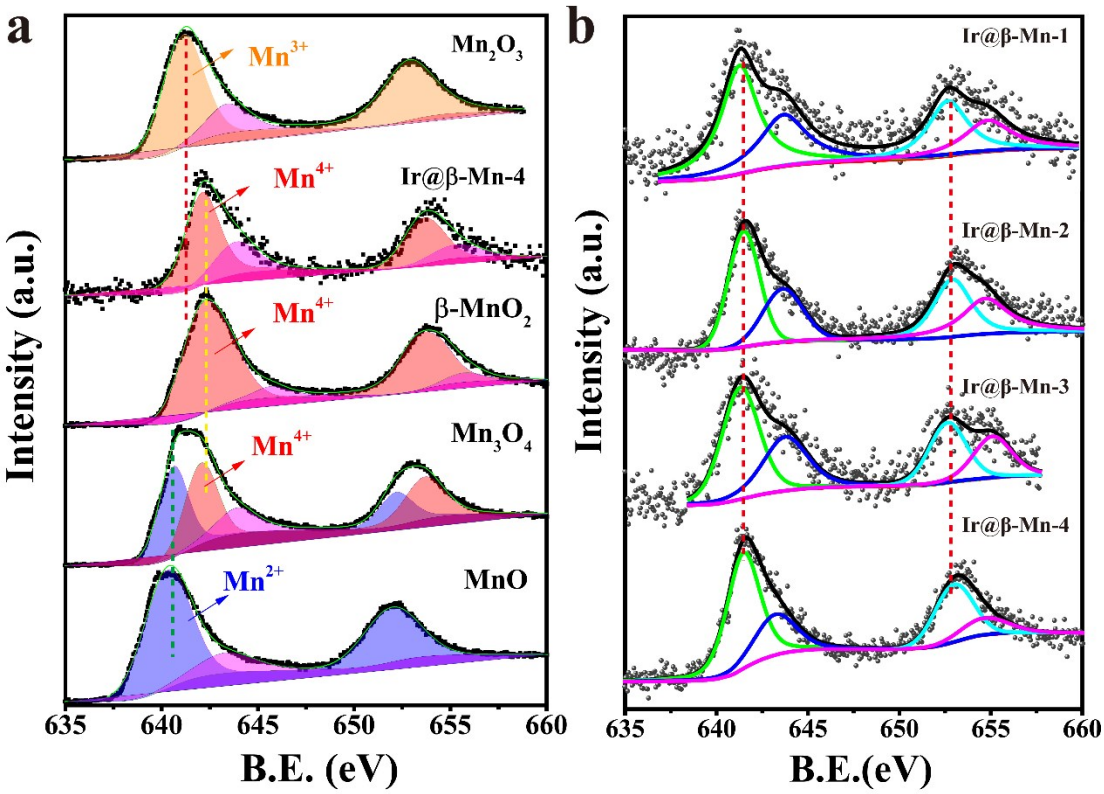

Figure S12. (a) The comparison of Mn-2p XPS of different Mn-based oxides. The binding energy of Mn-2$p_{3/2}$ strongly dependent onto the Mn valence states. The binding energy of Mn-2$p_{3/2}$ in prepared Ir@β-Mn-4 is closed to the Mn^{4+}. (b) The Mn-2p XPS of prepared Ir@Mn hybrid with different IrO_2 growth mass. By comparison, we can find that the valence states of support have no obvious change. The Mn-based oxides are purchased from the Macklin Co. Ltd., China, except the β-MnO_2.

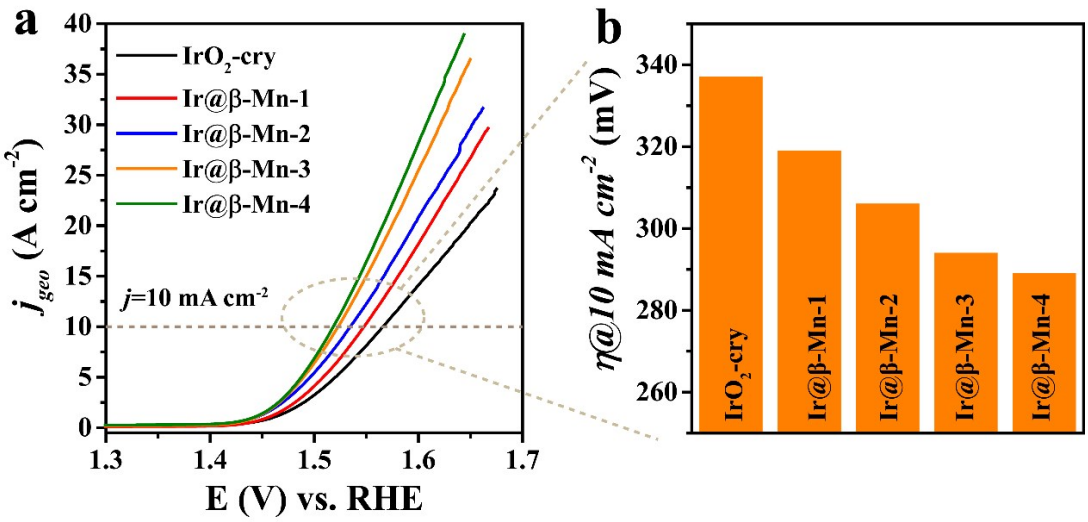

Figure S13. (a) Geometric OER activity of different materials. (b) The required overpotential of prepared materials at 10 mA cm^{-2}. All measurements are performed in 0.1 M $HClO_4$ at a scan rate of 10 mV s^{-1}. The *iR* loss from the solution resistance is corrected. Catalyst loading mass was ~0.2 mg cm^{-2}, and electrode area was 0.25 cm^2.

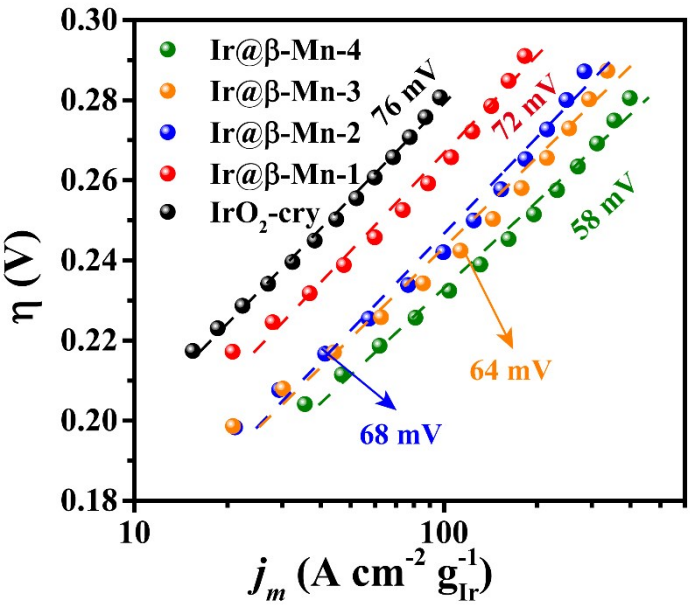

Figure S14. The Tafel plots of different materials.

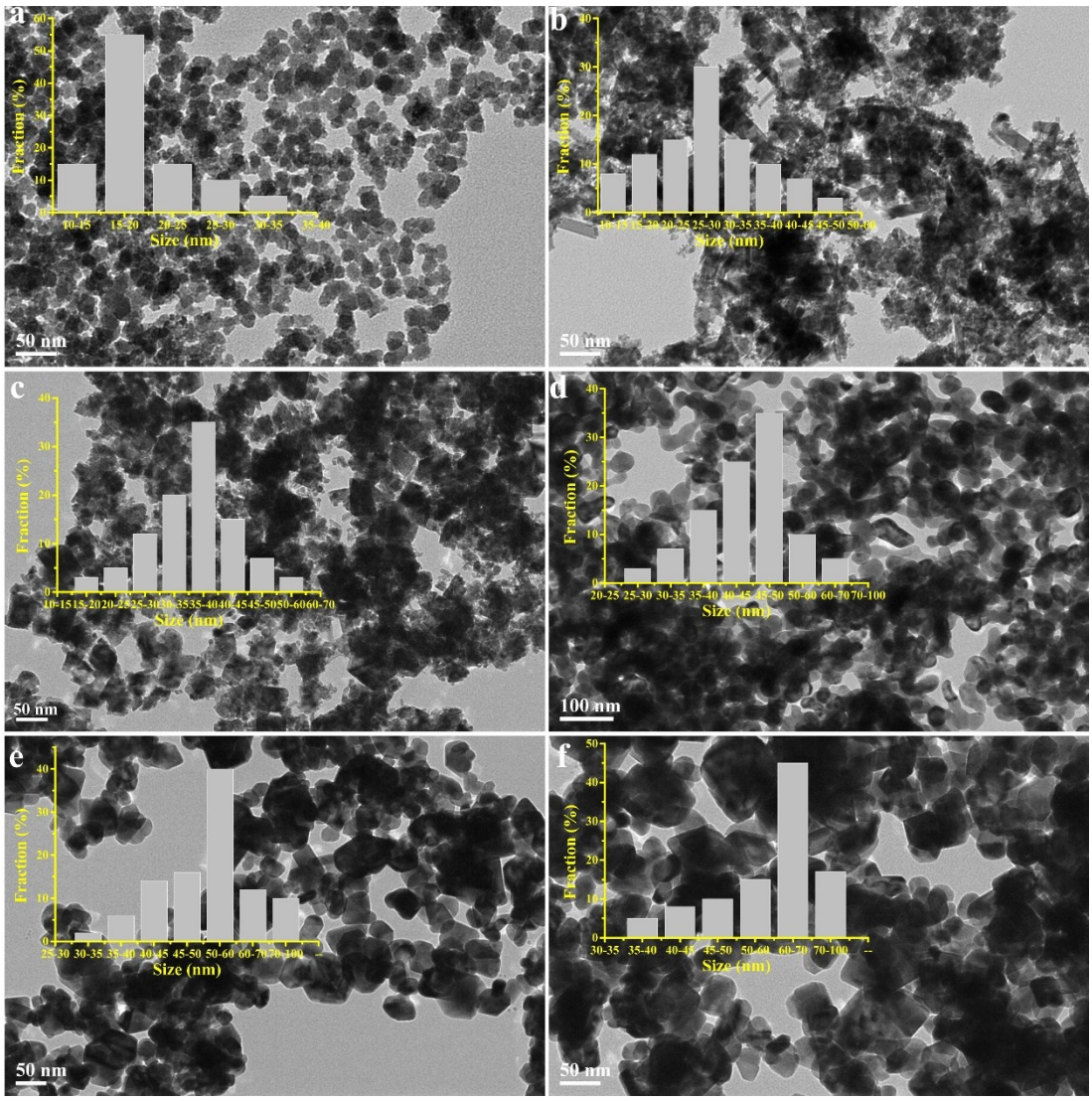

Figure S15. TEM images of prepared different IrO2 NPs, who are calcined at different temperature. (a)-(f) are the 200 ºC, 400 ºC, 500 ºC, 600 ºC, 700 ºC and 800 ºC, respectively.

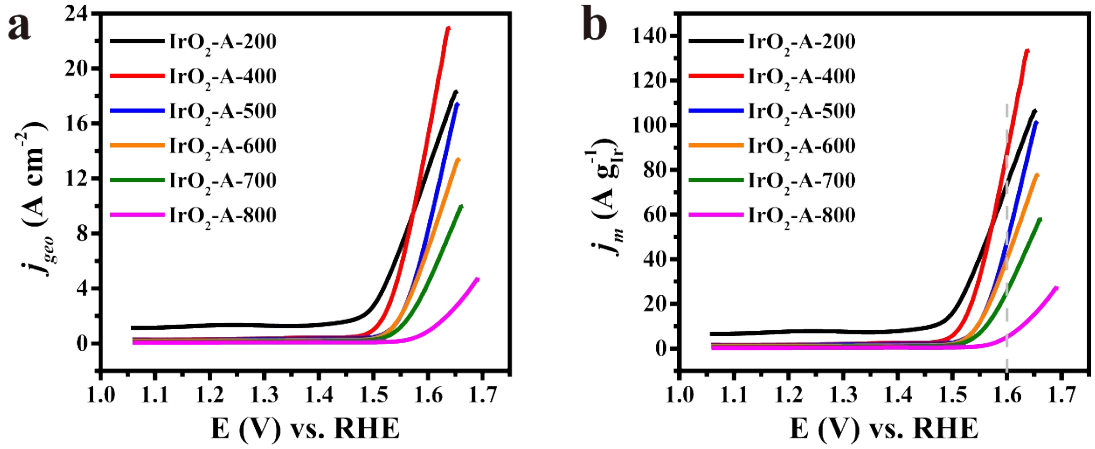

Figure S16. Geometric and mass activity of different IrO_2 materials. A-X (X=no.) means annealed at different temperature (°). All measurements are performed in 0.1 M $HClO_4$ at a scan rate of 10 mV s^{-1}. The *iR* loss from the solution resistance is corrected. Catalyst loading mass was ~0.2 mg cm^{-2}, and electrode area was 0.25 cm^2.

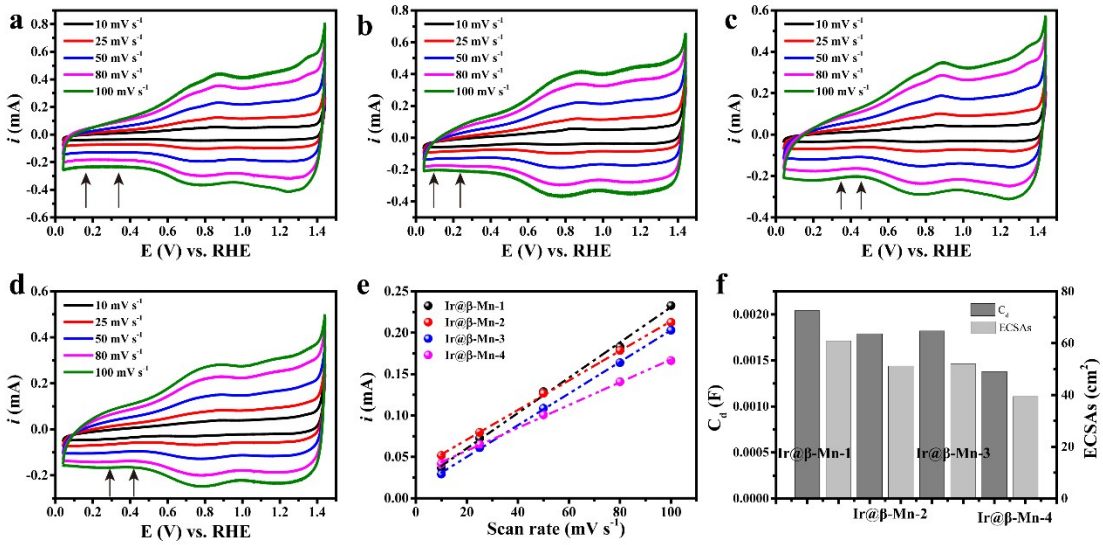

Figure S17. (a)-(d) are the CV curves of prepared Ir@β-Mn hybrids, corresponding in order are the Ir@β-Mn-1, Ir@β-Mn-2, Ir@β-Mn-3 and Ir@β-Mn-4, respectively. (e) The linear fitting of capacitive current with scan rate. (f) The calculated ECSAs of prepared hybrids. All measurements are performed in 0.1 M $HClO_4$ within the water oxidation window at different scan rate. The calculated ECSAs of different hybrids by using the arrow marked region in CV curves, in where no obvious Faradic current. The current determined by CV method includes two parts, capacitor current (i_c) and Faradic current (i_F); i_c is linear based on the scan rate determined by $i_c=C_d \cdot \nu$. The parameter C_d is crucial factor associated with electrochemical active sites. Thus, it can be normalized by $i/\nu = C_d$ (constant) $+i_F/\nu$ both obtaining the C_d value and marked Faradic current to determine the onset potential of OER activity. The region between vertical orange lines is chosen to estimate C_d value. ECSAs = C_d/C_s, where C_s=0.035 mF cm^{-2} based on the reported value[12]. The loading mass of catalysts is 0.2 mg cm^{-2} in all samples.

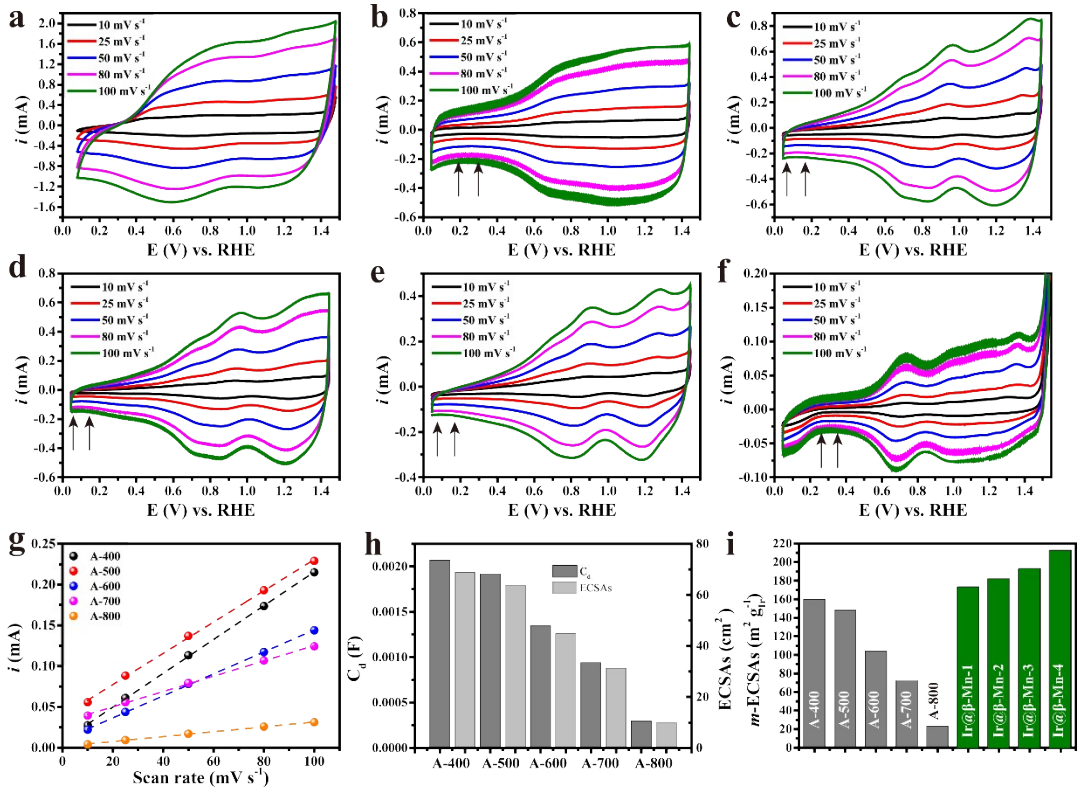

Figure S18. (a)-(f) are the CV curves of prepared different IrO_2 NPs, corresponding in order are the A-200, A-400, A-500, A-600, A-700 and A-800, respectively. (g) The linear fitting of capacitive current with scan rate. Due to the A-200 belongs to amorphous and its CVs are too broad, thus we do not consider its ECSA. (h) The calculated ECSAs of prepared IrO_2. (i) Normalized ECSAs by Ir mass. All measurements are performed in 0.1 M $HClO_4$ within the water oxidation window at different scan rate. The calculated ECSAs of different IrO_2 samples by using the arrow marked region in CV curves, in where no obvious Faradic current.

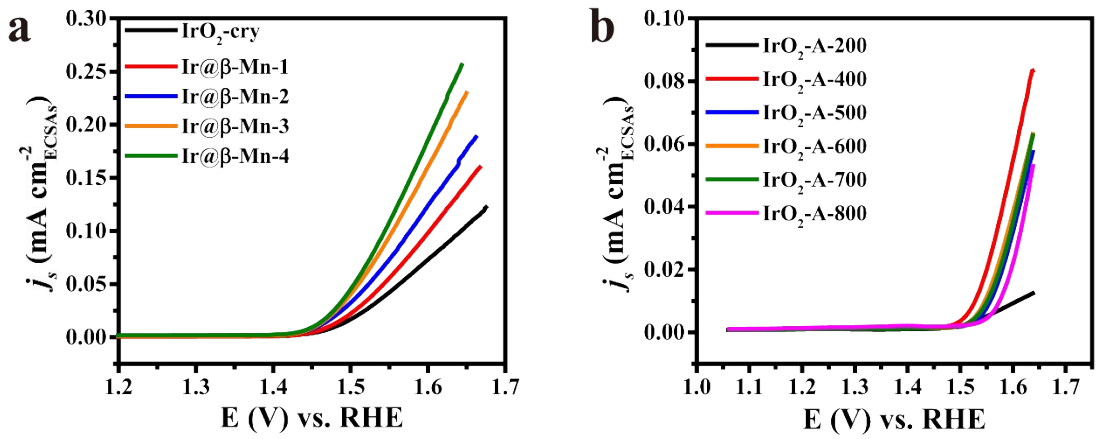

Figure S19. Specific activity of prepared different materials. (a) for prepared Ir@β-Mn hybrids and IrO_2-cry as a reference. (b) for different IrO_2 materials. A-X (X=no.) means annealed at different temperature (º). The IrO_2-cry is the sample of A-400. All measurements are performed in 0.1 M $HClO_4$ at a scan rate of 10 mV s^{-1}. The *iR* loss from the solution resistance is corrected. Catalyst loading mass was ~0.2 mg cm^{-2}, and electrode area was 0.25 cm^2.

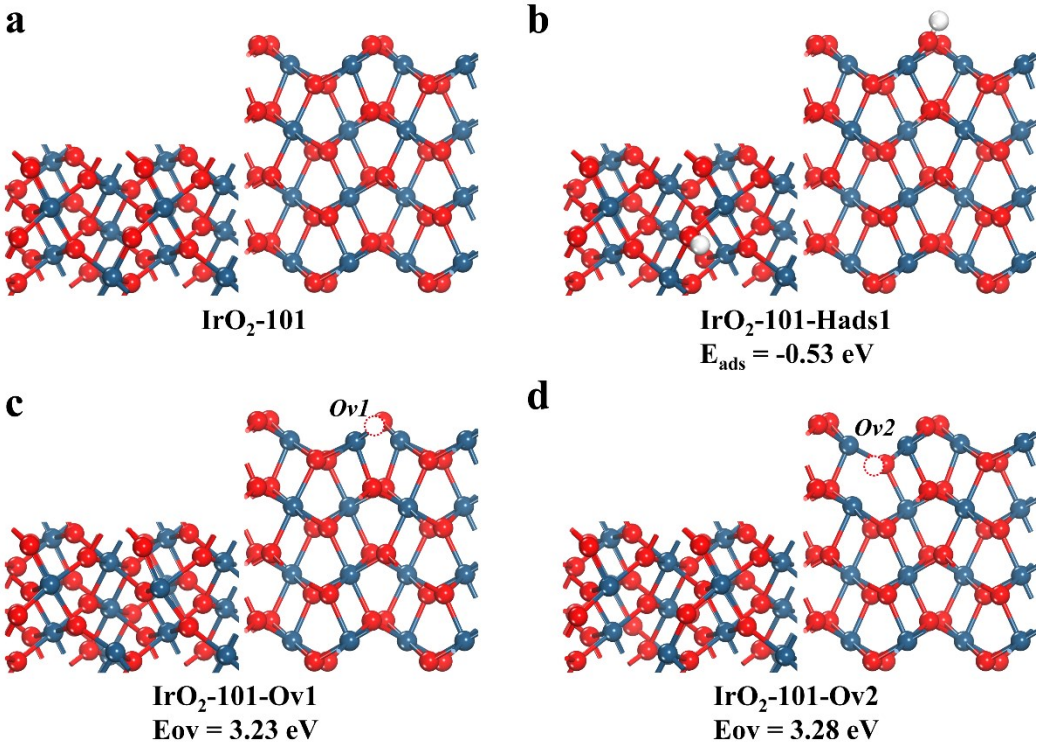

Figure S20. (a) The complete crystallography of IrO_2. (b) The surface hydroxylation on (101) plane and calculated adsorption energy of H. (c) The crystallography of IrO_2 when created an oxygen vacancy, the position of Ov corresponding to the Ir1-O1 path. The calculated formation energy of O_{v1} is 3.23 eV. (d) The crystallography of IrO_2 when created an oxygen vacancy on apical direction in IrO6 octahedron. The calculated formation energy of O_{v2} is 3.28 eV.

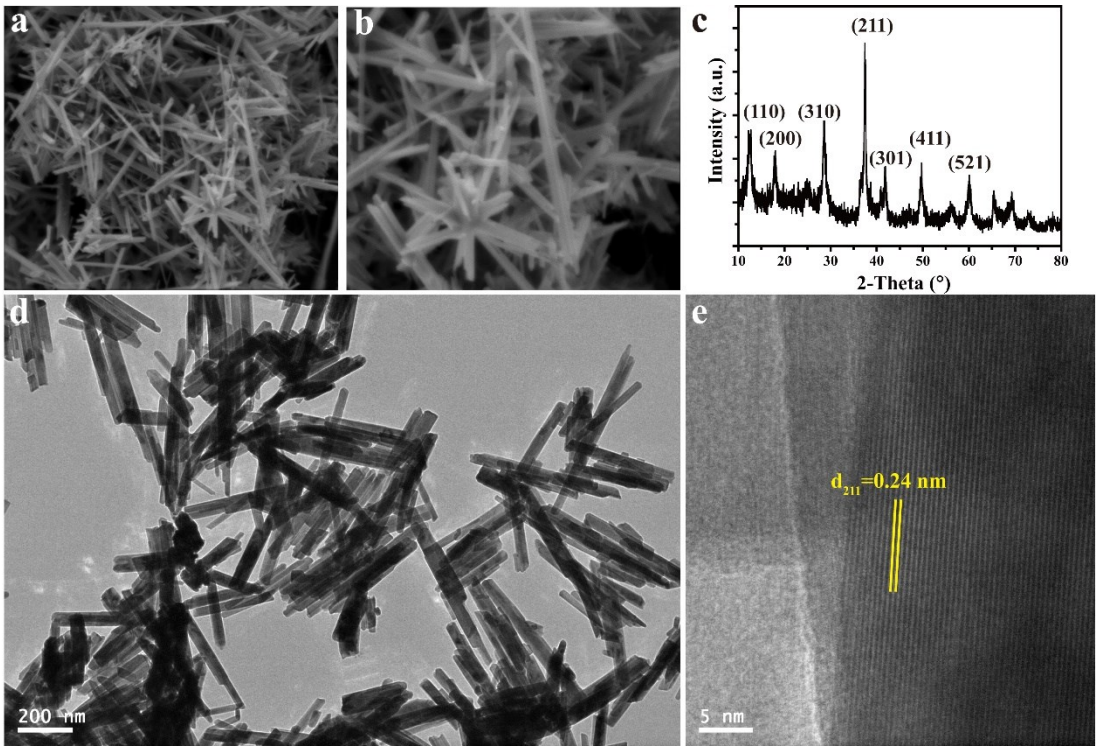

Figure S21. (a)-(b) SEM images of prepared rod-shaped α-MnO_2. (c) The XRD pattern of α-MnO_2, from the diffraction peaks positions, we can confirm it belongs to α-MnO_2. (d)-(e) TEM and HRTEM images of the α-MnO_2, the length of rod range of 200-600 nm, which below the β-MnO_2.

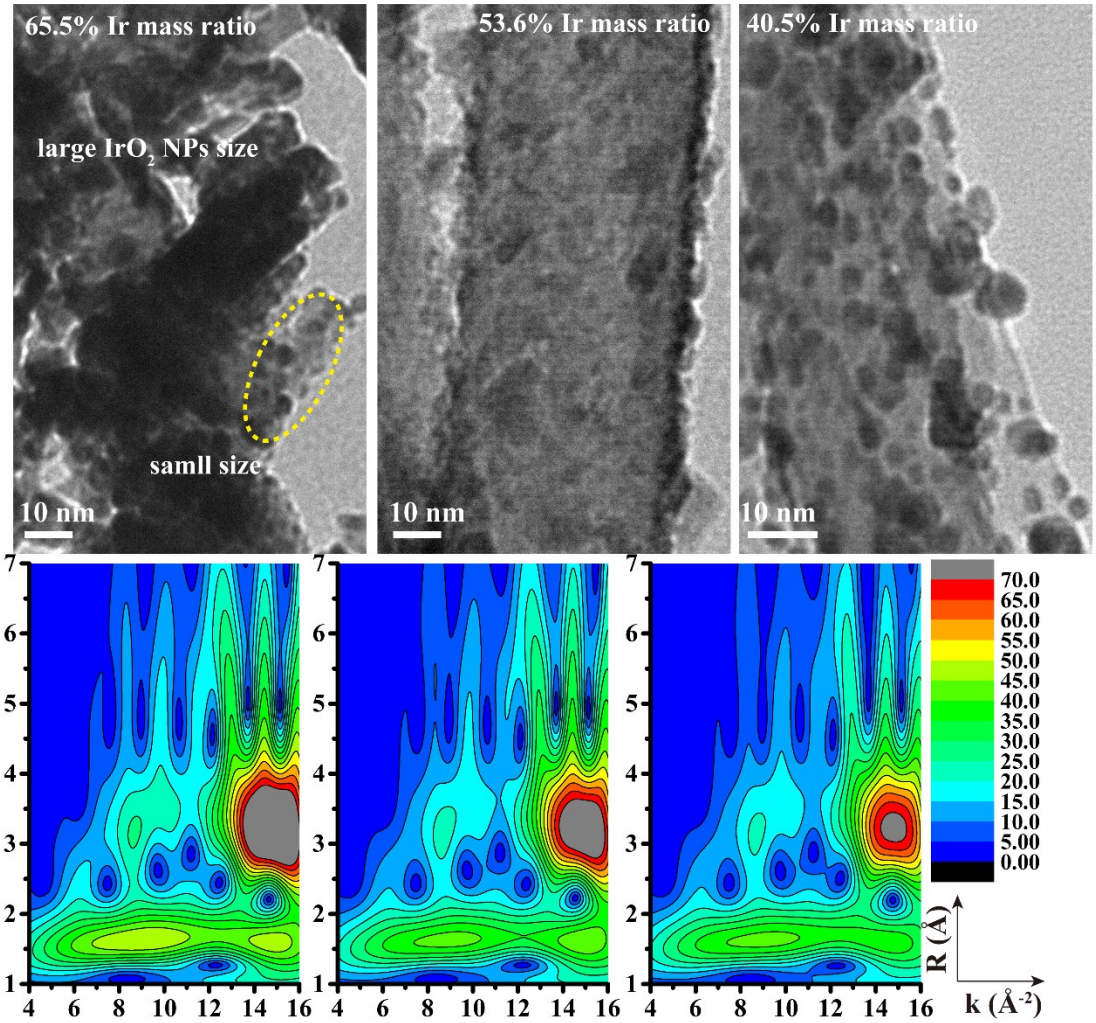

Figure S22. Structure evolution of Ir@α-Mn hybrid by HRTEM and EXAFS combined with M-WT.

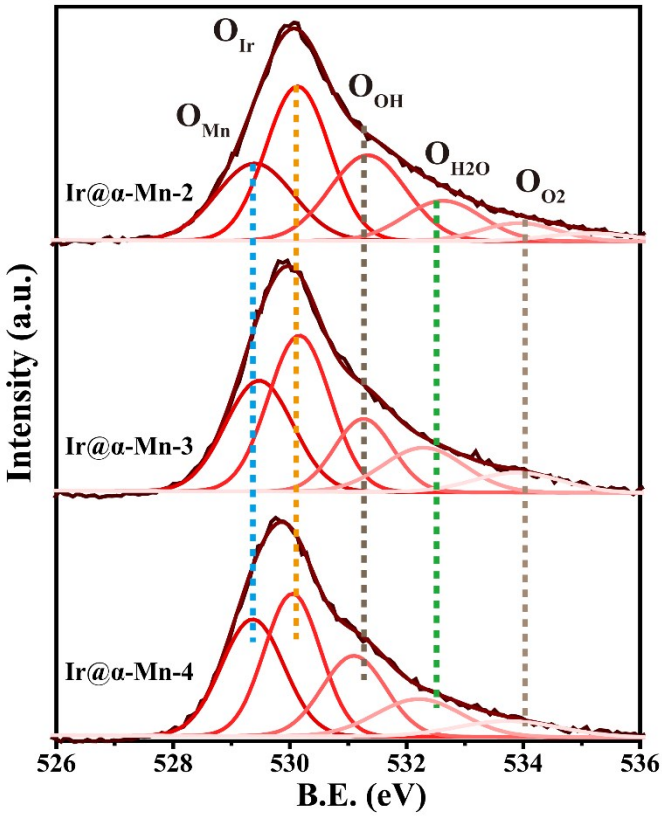

	O_{Mn} (%)	O_{Ir} (%)	O_{OH} (%)	O_{H2O} (%)
Ir@α-Mn-2	21	36	24	11
Ir@α-Mn-3	24	35	16	13
Ir@α-Mn-4	27	32	20	13

Figure S23. The XPS spectra of O-1s for prepared Ir@α-Mn hybrid. The binding energy is calibrated by C-1s with 284.6 eV. The Table placed on the bottom shows the area percentage of different O-species.

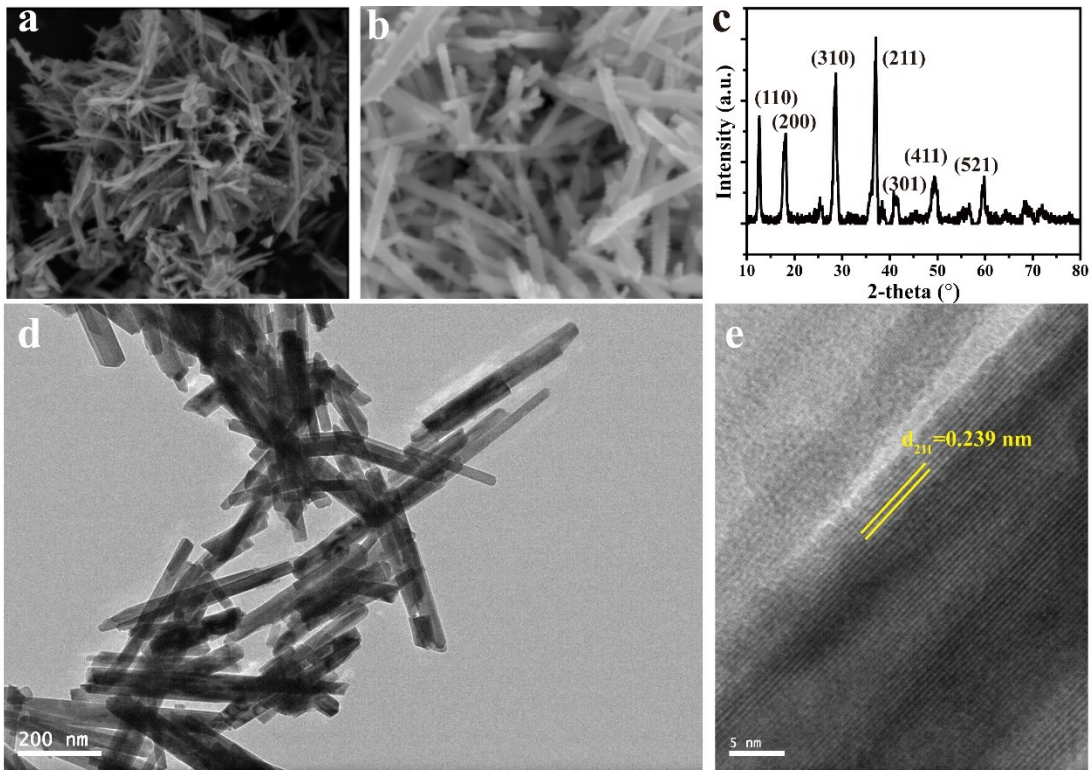

Figure S24. (a)-(b) SEM images of prepared rod-shaped cryptomelane (K_xMnO_2, k-Mn). (c) The XRD pattern of K_xMnO_2, from the diffraction peaks positions, we can confirm it belongs to $K_{1.66}Mn_8O_{16}$. (d)-(e) TEM and HRTEM images of the K_xMnO_2, the length of rod range of 400-800 nm, which also below the β-MnO_2.

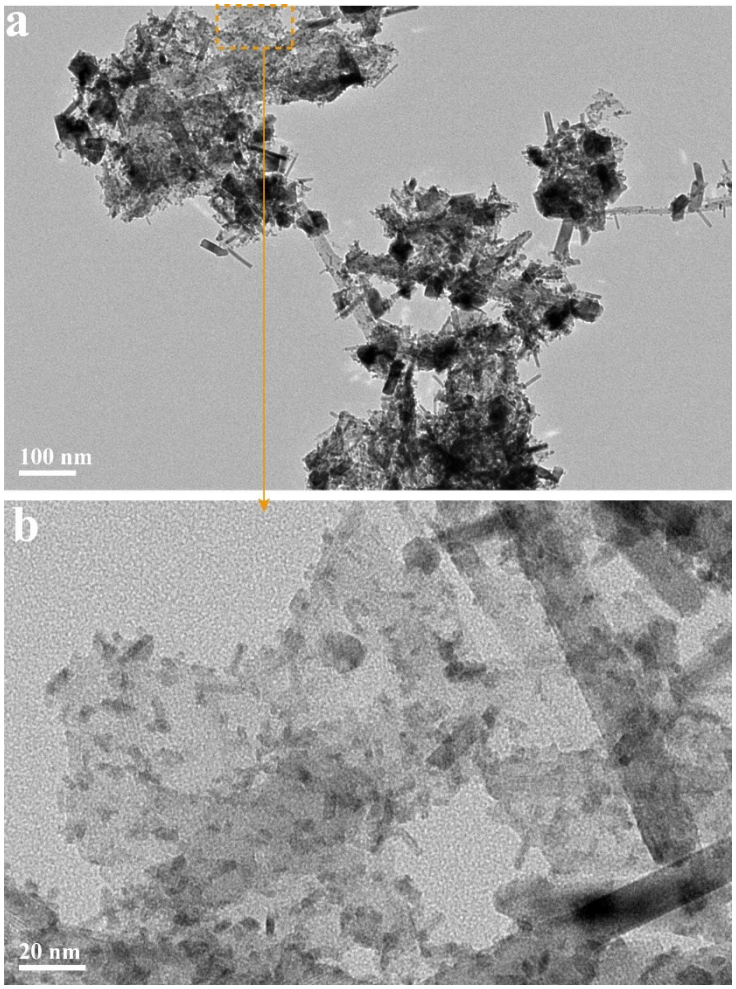

Figure S25. (a) HRTEM image of Ir@k-Mn-4, the growth of IrO_x NPs on the surface of k-Mn is not very uniform, and part of the IrO_x does not grow on the surface.

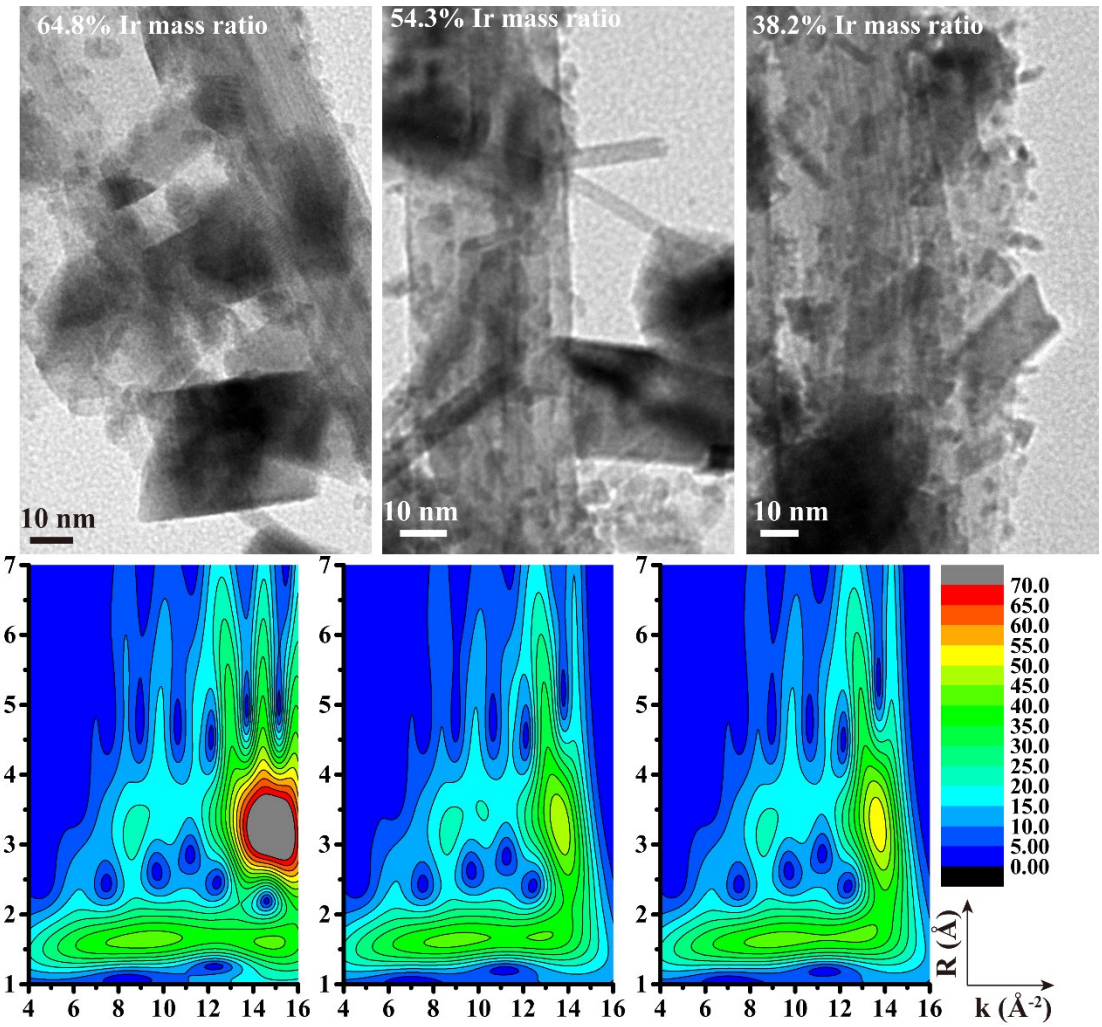

Figure S26. Structure evolution of Ir@k-Mn hybrid by HRTEM and EXAFS combined with M-WT.

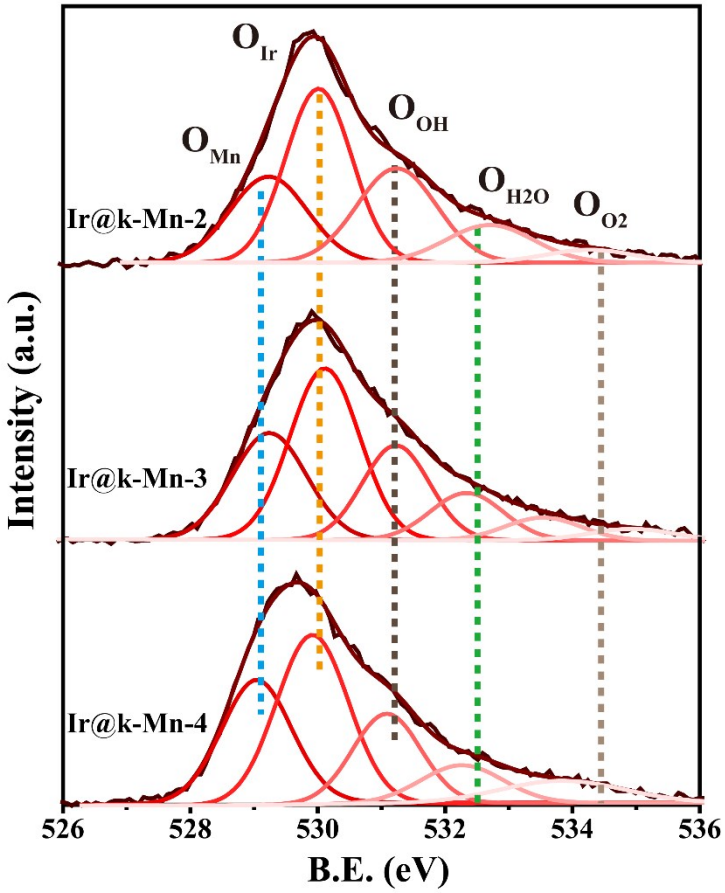

	O_{Mn} (%)	O_{Ir} (%)	O_{OH} (%)	O_{H2O} (%)
Ir@k-Mn-2	23	38	25	11
Ir@k-Mn-3	30	36	20	10
Ir@k-Mn-4	32	34	18	9

Figure S27. The XPS spectra of O-1s for prepared Ir@k-Mn hybrid. The binding energy is calibrated by C-1s with 284.6 eV. The Table placed on the bottom shows the area percentage of different O-species.

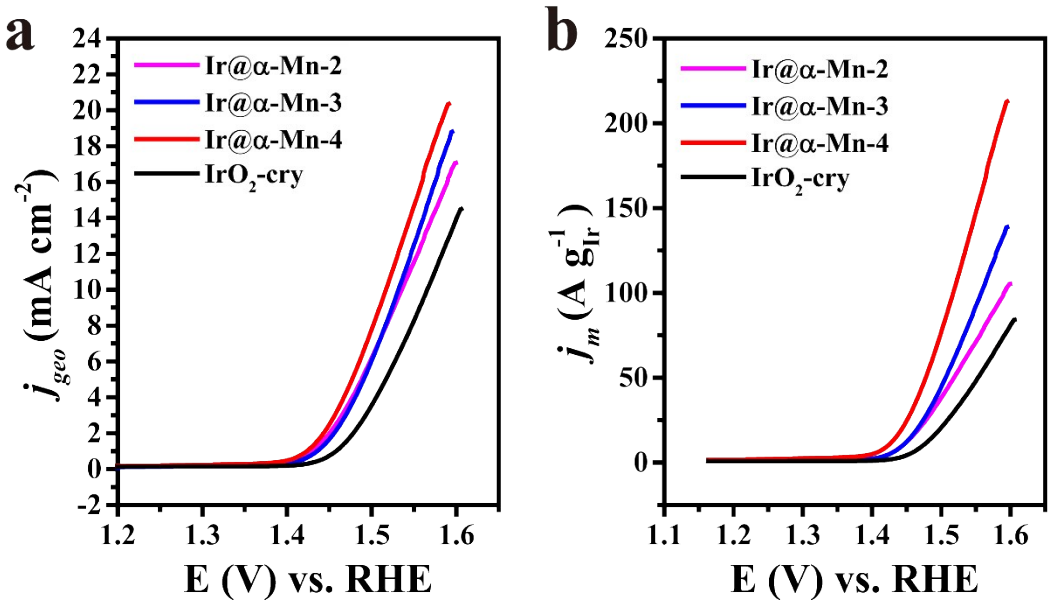

Figure S28. Evaluation of OER activity for Ir@α-Mn hybrids by electrochemical measurements. (a) Geometric activity and (b) mass activity of different materials. All measurements are performed in 0.1 M $HClO_4$ at a scan rate of 10 mV s^{-1}. The *iR* loss from the solution resistance is corrected. Catalyst loading mass was ~0.2 mg cm^{-2}, and electrode area was 0.25 cm^2.

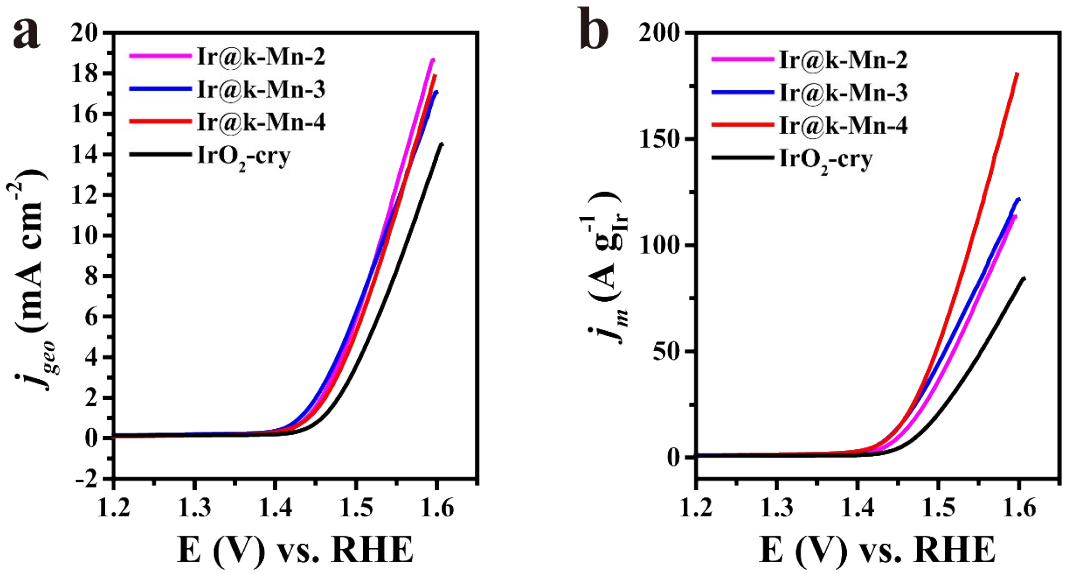

Figure S29. Evaluation of OER activity for Ir@k-Mn hybrid by electrochemical measurements. (a) Geometric activity and (b) mass activity of different materials. All measurements are performed in 0.1 M $HClO_4$ at a scan rate of 10 mV s^{-1}. The *iR* loss from the solution resistance is corrected. Catalyst loading mass was ~0.2 mg cm^{-2}, and electrode area was 0.25 cm^2.

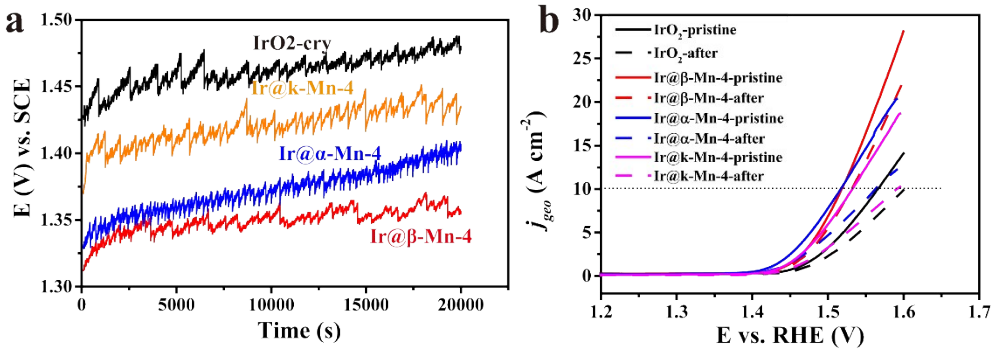

Figure S30. (a) Chronopotentiometric curves of IrO_2 supported hybrids in 0.1 M $HClO_4$ solution at 10 mA cm^{-2}(geo) for OER (without *iR* compensations). (b) The compared OER performance of prepared materials before and after stability tests.

Table S5. The determined metal ions concentration in electrolyte by ICP-MS after durability test.

Catalysts	Ir concentration ($mg\ L^{-1}$)	Mn concentration ($mg\ L^{-1}$)	Ir dissolved (%)	Mn dissolved (%)
IrO_2-cry	0.036	\	2.5	\
Ir@β-Mn-4	0.023	0.049	3.7	7.2
Ir@α-Mn-4	0.045	0.077	7.2	11.4
Ir@k-Mn-4	0.050	0.112	7.9	17.3

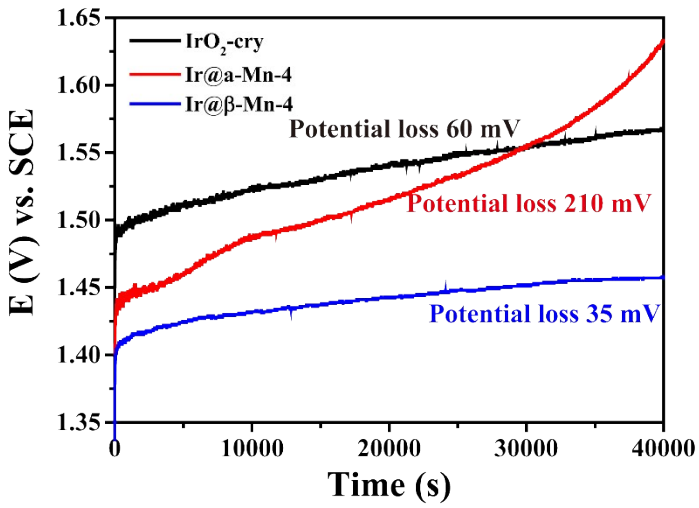

Figure S31. Stability tests of IrO_2 supported hybrids in 0.1 M $HClO_4$ solution at 20 mA cm^{-2}(geo) for OER (without *iR* compensations). In order to accelerate the elimination of bubbles from the surface of the electrode, we adopted the method of magnetically stirring the solution. The curves are smoothed. Here, we can find that Ir@β-Mn-4 shows better stability than Ir@α-Mn-4 at the same amount of IrO_2 growth. Surface coverage is decisive for the stability of supported IrO_x hybrids.

References:

(1) Zheng, D.; Sun, S.; Fan, W.; Yu, H.; Fan, C.; Cao, G.; Yin, Z.; Song, X. One-Step Preparation of Single-Crystalline β-MnO2 Nanotubes. *The Journal of Physical Chemistry B* **2005,** *109* (34), 16439-16443, DOI: 10.1021/jp052370l.

(2) Davis, D. J.; Lambert, T. N.; Vigil, J. A.; Rodriguez, M. A.; Brumbach, M. T.; Coker, E. N.; Limmer, S. J. Role of Cu-Ion Doping in Cu-α-MnO2 Nanowire Electrocatalysts for the Oxygen Reduction Reaction. *J. Phys. Chem. C* **2014,** *118* (31), 17342-17350, DOI: 10.1021/jp5039865.

(3) Lambert, T. N.; Vigil, J. A.; White, S. E.; Delker, C. J.; Davis, D. J.; Kelly, M.; Brumbach, M. T.; Rodriguez, M. A.; Swartzentruber, B. S. Understanding the effects of cationic dopants on α-MnO2 oxygen reduction reaction electrocatalysis. *J. Phys. Chem. C* **2017,** *121* (5), 2789-2797.

(4) Chen, K.; Wang, M.; Li, G.; He, Q.; Liu, J.; Li, F. Spherical α-MnO2 Supported on N-KB as Efficient Electrocatalyst for Oxygen Reduction in Al–Air Battery. *Materials* **2018,** *11* (4), 601.

(5) Sun, W.; Cao, L.-m.; Yang, J. Conversion of inert cryptomelane-type manganese oxide into a highly efficient oxygen evolution catalyst via limited Ir doping. *Journal of Materials Chemistry A* **2016,** *4* (32), 12561-12570.

(6) YU Hai-Sheng, W. X.-J., LI Jiong, GU Song-Qi, ZHANG Shuo, WANG Li-Hua, MA Jing-Yuan, LI Li-Na, GAO Qian, SI Rui, SUN Fan-Fei, WANG Yu, SONG Fei, XU Hong-Jie, YU Xiao-Han, ZOU Yang, WANG Jian-Qiang, JIANG Zheng, HUANG Yu-Ying. The XAFS beamline of SSRF. *Nucl. Sci. Tech.* **2015,** *26* (5), 050102, DOI: 10.13538/j.1001-8042/nst.26.050102.

(7) Kresse, G.; Furthmüller, J. Efficient iterative schemes for ab initio total-energy calculations using a plane-wave basis set. *Physical review B* **1996,** *54* (16), 11169.

(8) Blöchl, P. E. Projector augmented-wave method. *Physical review B* **1994,** *50* (24), 17953.

(9) Perdew, J. P.; Burke, K.; Ernzerhof, M. Generalized Gradient Approximation Made Simple. *Phys. Rev. Lett.* **1996,** *77* (18), 3865-3868.

(10) Teter, M. P.; Payne, M. C.; Allan, D. C. Solution of Schrödinger's equation for large systems. *Physical Review B* **1989,** *40* (18), 12255.

(11) Bolzan, A. A.; Fong, C.; Kennedy, B. J.; Howard, C. J. Structural Studies of Rutile-Type Metal Dioxides. *Acta Crystallogr.* **1997,** *53* (3), 373–380.

(12) McCrory, C. C. L.; Jung, S.; Peters, J. C.; Jaramillo, T. F. Benchmarking Heterogeneous Electrocatalysts for the Oxygen Evolution Reaction. *J. Am. Chem. Soc.* **2013,** *135* (45), 16977-16987, DOI: 10.1021/ja407115p.